How to Cite: Milusheva, R.Yu., Nurgaliev, I.N., Abilkasimov, A.B., & Rashidova, S.Sh. (2025). Bioactive Chitosan/β-Tricalcium Phosphate Coatings on Titanium: Experimental Optimization and DFT Insight. *Eurasian Journal of Chemistry, 30, 4(120), 45–65.* https://doi.org/10.31489/2959-0663/4-25-12

Article

Received: 19 August 2024 | Revised: 27 November 2024 | Accepted: 2 December 2024 | Published online: 9 December 2024

UDC 615.03+ 661.632.2+544.18

https://doi.org/10.31489/2959-0663/4-25-12

Rakiya Yu. Milusheva[1], Ilnar N. Nurgaliev[1*], Akmal B. Abilkasimov[2], Sayora Sh. Rashidova[1]

[1]*Institute of Polymer Chemistry and Physics of the Academy of Sciences of the Republic of Uzbekistan, Tashkent, Uzbekistan;*
[2]*Kimyo International University in Tashkent, Tashkent, Uzbekistan*
*(*Corresponding author's e-mail: ilnarvodnik@gmail.com)*

Bioactive Chitosan/β-Tricalcium Phosphate Coatings on Titanium: Experimental Optimization and DFT Insight

The development of bioactive coatings combining biopolymers and calcium phosphate ceramics offers an effective strategy to improve osseointegration and functional performance of titanium-based implants. In this study, highly purified Bombyx mori chitosan (CS-BM) and β-tricalcium phosphate (β-TCP) were used to fabricate hybrid coatings on titanium substrates via electrochemical deposition under optimized conditions (52 °C, pH 6.6–7.0, 2.0–4.0 mA·cm^{-2}). SEM and AFM analyses revealed uniform, strongly adherent two-layer structures with microtopography (1–10 μm roughness) favorable for bone ingrowth, while elemental analysis confirmed complete Ca- and P-rich coverage. Density functional theory (DFT) modeling confirmed the cooperative role of Ca^{2+} and PO_4^{3-} in bridging CS-BM to TiO_2, contributing to coating stability. In vivo studies demonstrated that CS-BM/TCP-coated implants accelerated early contact osteogenesis, dense trabecular bone formation, and stable bone–implant integration compared to uncoated controls. In an experimental osteoporosis model, intramuscular administration of CS-BM with active calcium or calcium–vitamin D_3 significantly enhanced fibroblast-to-osteoblast differentiation, stimulated osteoid synthesis, and led to complete restoration of bone microarchitecture within 21 days. These findings highlight CS-BM/TCP coatings as a sustainable, locally sourced, and highly effective platform for orthopedic and dental implant applications, with additional therapeutic potential in osteoporosis management.

Keywords: chitosan, Bombyx mori, DFT modeling, chitosan coating, β-tricalcium phosphate, TiO_2(110), electrochemical deposition, implant, osteogenesis

Buketov University

Introduction

The design of bioactive surfaces for titanium-based implants remains a pivotal objective in contemporary biomedical materials research. Titanium and its alloys are extensively employed in orthopedic and dental applications owing to their excellent mechanical performance, corrosion resistance, and intrinsic biocompatibility. Nevertheless, the inherently bioinert nature of their surfaces restricts direct bonding with bone tissue, thereby limiting long-term clinical performance. To overcome this limitation, extensive efforts have been directed toward surface functionalization strategies that integrate biopolymers with calcium phosphate ceramics, aiming to enhance osseointegration and biological activity [1–10].

One of the key challenges in biomedical materials science is enhancing the physico-mechanical and biological performance of implants to improve their long-term biocompatibility. A widely adopted approach to achieving this goal is the surface modification of the underlying implant material. Among the diverse materials investigated for such applications, chitosan (CS), a β-(1→4)-linked D-glucosamine polysaccharide, has garnered considerable attention due to its intrinsic biocompatibility, biodegradability, and strong affinity for biological molecules via its amino and hydroxyl functional groups. These characteristics make CS a particularly promising candidate for advanced prosthetic applications, positioning it at the forefront of bioactive surface engineering strategies [11–14].

Globally, the production of chitin and its derivative, CS, is predominantly based on shellfish exoskeletons as the primary raw material source. However, this approach is constrained by seasonal and geographic limitations in shellfish harvesting, which restrict large-scale and consistent supply. In Uzbekistan, where sericulture has been historically well-developed, an alternative and underutilized resource is available in the form of Bombyx mori silkworm pupae—by-products of the silk production process. These pupae represent a sustainable source of chitin that can be chemically processed into CS, a polymer of equally high industrial and biomedical value [15–21].

© 2025 The Authors. This is an open access article under the CC BY-NC-ND license (http://creativecommons.org/licenses/by-nc-nd/4.0/)

Tricalcium phosphate (TCP), particularly in its β-phase, is a well-recognized osteoconductive material extensively applied in bone regeneration owing to its close compositional resemblance to the mineral phase of natural bone. Compared with hydroxyapatite, β-tricalcium phosphate demonstrates more favorable resorption kinetics and pronounced osteoinductive potential, which makes it especially suitable for use in coating systems designed to enable controlled ion release and facilitate progressive bone remodeling [22, 23].

Recent research has increasingly focused on combining CS with TCP to develop composite materials that provide both structural reinforcement and enhanced biological functionality. Among the various deposition techniques, electrochemical methods are particularly attractive for producing uniform, strongly adherent coatings under low-temperature conditions [24]. Literature reports indicate that promising coating components include phosphate, calcium, copper, and gold ions, as well as macromolecular bioactive polymers such as CS, fibroin, and TCP [25–32]. Comprehensive investigations into the use of these constituents in implant coatings are regarded as highly promising, with the potential to markedly improve both the mechanical performance and the biological activity of dental implant surfaces.

Given the high incidence and increasing frequency of bone fractures—driven in part by technological progress and industrialization—post-traumatic osteoporosis has become increasingly prevalent. Recent studies have emphasized the important role of CS in bone tissue metabolism and in the treatment of osteoporosis of various etiologies [33–36]. Composite coatings combining chitosan with calcium phosphate significantly enhance cell adhesion and osteoblastic differentiation (e.g., MG‑63, MC3T3‑E1), while increasing surface hydrophilicity—key properties for improved osseointegration [37]. CS is of particular interest as a potential therapeutic agent for osteoporosis due to its ability to enhance calcium absorption, stimulate bone formation, and provide targeted drug delivery. CS-calcium complexes for osteoporosis treatment are especially promising owing to their biocompatibility, drug delivery potential, and osteogenic properties. An underexplored alternative to conventional marine-sourced chitosan is Bombyx mori chitosan, which, due to its lower crystallinity, high purity, and enhanced solubility, offers unique advantages for biomedical coatings; given the growing demand for sustainable, locally available biomaterials and the complete absence of studies applying CS-BM in implant surface engineering, its investigation is both timely and scientifically relevant. Despite promising experimental advances, a detailed understanding of the interactions at the atomic level between coating components and titanium dioxide surfaces remains limited. Density functional theory (DFT) and atomistic modeling can provide insights into surface binding, charge redistribution, and electronic effects, offering valuable guidance for experimental design.

This study aims to develop and optimize electrochemically deposited chitosan *Bombyx mori*/β-tricalcium phosphate (CS-BM/TCP) hybrid coatings on titanium substrates, elucidating their interfacial binding mechanisms and evaluating their potential to enhance osseointegration and bone regeneration. The experimental approach is complemented by DFT simulations of the rutile TiO_2(110) surface, focusing on its interactions with individual and cooperative adsorbates, including a chitosan dimer, Ca^{2+}, and PO_4^{3-} ions. This combined methodology aims to elucidate the underlying binding mechanisms responsible for improved coating adhesion and enhanced bioactivity.

Experimental

Isolation of Chitin from Bombyx mori and Synthesis of Chitosan.

The first stage of chitin production involves multiple extractions of oil using organic solvents, including ethanol, at elevated temperature. Chitin was extracted from *Bombyx mori* silkworm pupae using 5–7 % NaOH or KOH solutions (1:10 ratio) at 90 °C for 3 hours, followed by extensive washing and drying. Proteins are removed by treating the defatted raw material with an alkali solution. Chitosan *Bombyx mori* (CS-BM) was obtained by deacetylating chitin in 50 % NaOH (1:10 ratio) at 120 °C for 3 h. The resulting product was washed to neutrality, lyophilized at –50 °C under 0.5 mbar pressure, yielding a yellowish powder readily soluble in 2 % acetic acid. Purification involved dissolving crude CS-BM in 2 % acetic acid, coagulating at controlled pH, washing with ethanol, centrifugation, and subsequent lyophilization, as described previously.

Characterization Techniques

The characterization of the obtained samples was carried out using a set of complementary analytical techniques. Fourier transform infrared (FTIR) spectra were acquired with a Shimadzu 84005 spectrometer (Japan) in the range of 4000–400 cm^{-1} using KBr pellet preparation. The phase composition was analyzed by

Buketov University

X-ray diffraction (XRD) on a Rigaku Miniflex 600 diffractometer (Japan) employing Cu Kα radiation (λ = 1.5406 Å). The elemental composition was determined with a Flash Smart elemental analyzer (Thermo Scientific, USA). Surface topography was examined by atomic force microscopy (AFM) using an Agilent Technologies 5500 system (USA), while morphological features were observed by scanning electron microscopy (SEM) on an EVO MA10 instrument (ZEISS, Germany).

Preparation of Electrolyte Solutions and Coating Deposition

The electrolyte solution was prepared by dissolving chitosan derived from CS-BM, 0.5 g L^{-1} in 2 % acetic acid, followed by mixing with a saturated 0.2 M TCP solution. Titanium plates (30×10×1 mm, surface roughness 4.0 μm) were thoroughly cleaned and subsequently immersed in the prepared electrolyte. Electrochemical deposition was carried out at 52 °C for 15 h under a constant current density of 2.0–4.0 $mA \cdot cm^{-2}$ in a pH 6.6–6.7 buffer solution. Previous studies have demonstrated that lower pH values (<6.5) negatively impact the adhesion strength of calcium phosphate coatings, primarily due to the accelerated dissolution of precursor species and reduced nucleation efficiency on titanium substrates [37, 38]. After electrolytic deposition, the titanium plates were rinsed thoroughly with demineralized water and dried in an oven at 50 °C for 12 h.

Biomedical Studies of Titanium Implantation in Vivo

The in vivo biomedical study was conducted on 18 clinically healthy, non-breed rabbits weighing 4200–4300 g. The animals were maintained under standard vivarium conditions at the Interuniversity Scientific Research Laboratory of the Tashkent Medical Academy and provided with a standard diet. All experimental procedures were performed in strict compliance with the international guidelines for the ethical treatment of laboratory animals, as outlined in the European Communities Council Directive 86/609/EEC of 24 November 1986.

Titanium dental implants coated with a bioactive TCP/CS-BM composite, as well as uncoated titanium implants, were surgically placed under general anesthesia. The animals were randomly assigned to three experimental groups:

Group 1 — Intact control;

Group 2 — Implant without bioactive coating;

Group 3 — Implant with bioactive coating.

General anesthesia was induced via intravenous injection of a freshly prepared sodium ethaminal solution (40 $mg \cdot kg^{-1}$) into the auricular vein. Upon achieving deep anesthesia, 0.5 % novocaine solution was administered subcutaneously at the surgical site. Osteoplastic surgery for implant insertion was performed using a 1 mm diameter drill operating at 1000 rpm under continuous saline irrigation. Implant placement was completed using a rotating torque key to ensure controlled insertion.

Postoperative monitoring of the animals' general condition was carried out hourly during the first 24 hours and subsequently once daily over a 90-day period. Radiographic assessments of the implant sites were performed at 1, 2, and 3 months post-surgery to evaluate the progression of osseointegration.

Biomedical Evaluation of Modified Chitosan for Osteoporosis Treatment

The biomedical evaluation of modified chitosan for osteoporosis treatment was conducted on 50 healthy female Chinchilla rabbits weighing 2.0–2.5 kg. Osteoporosis was experimentally induced by performing an osteotomy of the right femur, followed by immobilization of the limb. After 40–50 days, radiographic examinations confirmed the development of osteoporosis, and the animals were divided into three experimental groups. The first group (n = 10) served as the control and, after removal of immobilization, was kept under standard conditions without treatment. The second group (n = 15) received intramuscular injections of CS-BM combined with active calcium for 20 days, while the third group (n = 15) received CS-BM in combination with "Calcium-D3 Nycomed" for the same duration. At the end of the treatment period, all animals were euthanized, and samples from the femoral epiphysis and diaphysis were collected for micromorphological analysis. The specimens were fixed in 10 % neutral buffered formalin and decalcified in 5 % nitric acid in preparation for histological examination.

Statistical Analysis

The experimental data were processed statistically using Microsoft Excel software. Calculated parameters included the arithmetic mean (M), standard deviation (σ), standard error of the mean (m), and relative values expressed as percentages. Differences between mean values were evaluated for statistical significance

Buketov University

using Student's t-test, with a threshold of $p \leq 0.05$ considered significant. All statistical analyses were performed in accordance with established guidelines for the processing of clinical and laboratory research data.

Computational Details

Density functional theory (DFT) calculations were performed using the Vienna Ab-initio Simulation Package (VASP) [39–42]. The Perdew–Burke–Ernzerhof (PBE) generalized gradient approximation (GGA) [43] was used for the exchange-correlation functional, and projector augmented-wave (PAW) pseudopotentials [44] were employed.

A kinetic energy cutoff of 500 eV was chosen after convergence tests, ensuring total energy variation below 10^{-5} eV/atom. Brillouin zone sampling was performed using a Monkhorst–Pack grid [45] of 2×2×1 for the slab models. Atomic structures were fully optimized until the residual forces on each atom were less than 0.02 eV $Å^{-1}$.

The rutile TiO_2 structure was obtained from the Materials Project (mp-2657) and used as the model for the TiO_2(110) surface. The rutile TiO_2(110) surface was modeled as a 2×2 supercell slab composed of four atomic layers separated by a vacuum region of 20 Å along the surface normal (*z*-axis). The bottom two layers were fixed to represent the bulk structure, while the top layers were relaxed. Dipole corrections were applied along the *z*-direction (LDIPOL = TRUE, IDIPOL = 3) to eliminate artificial electrostatic interactions caused by asymmetry in the slab geometry.

The chitosan repeating unit was represented by the protonated glucosamine monomer ($[GlcNH_3]^+$), optimized separately in the gas phase. To maintain overall charge neutrality in periodic boundary conditions, a uniform compensating background charge was applied, following standard procedures for charged adsorbates [46]. This approach enables reliable estimation of local binding energetics and charge redistribution while avoiding long-range Coulomb artifacts.

Adsorption models included: (i) isolated $[GlcNH_3]^+$ interacting with TiO_2(110); (ii) single Ca^{2+} and PO_4^{3-} ions; and (iii) a cooperative CS–Ca^{2+}–PO_4^{3-} composite cluster. β-Tricalcium phosphate (β-TCP) was modeled in its rhombohedral R3c phase (space group No. 161) using crystallographic parameters from the ICSD database, cross-validated with data from the Materials Project (mp-3487).

The adsorption energy (E_{ads}) was calculated using:

$$E_{ads} = E_{(surface + adsorbate)} - E_{(surface)} - E_{(adsorbate)},$$

where $E_{(surface + adsorbate)}$ is the total energy of the adsorption system, and $E_{(surface)}$ and $E_{(adsorbate)}$ correspond to the isolated surface and molecule/ion, respectively.

Charge transfer analysis was performed using the Bader method [47, 48]. The chosen DFT-PBE/PAW level of theory provides a good balance between accuracy and computational efficiency for describing oxide–biomolecule interfaces and has been widely validated for TiO_2 and calcium phosphate systems [49]. Charge transfer was estimated using Bader charge analysis.

Results and Discussion

Physicochemical Properties of CS and TCP

For the purposes of this study—given the intended biomedical application—highly purified CS-BM was required. CS-BM purification was carried out according to a previously developed method [15, 16]. The physicochemical properties of the starting material were characterized using elemental analysis, IR spectroscopy, and X-ray diffraction. Additionally, the degree of deacetylation (DDA) and viscosity-average molecular weight (M_V) of the CS-BM samples were determined. Purified CS-BM exhibited high nitrogen content (8.52 %), low ash content (1.43 %), and high solubility in acetic acid (98.85 %). TCP powder displayed limited solubility in water but dissolved well in acetic acid, forming hydrophosphates.

FTIR spectra confirmed characteristic CS-BM functional groups (OH, NH_2, and C–O–C) and complete deacetylation. TCP spectra showed strong phosphate group vibrations, while XRD confirmed the crystalline phase of single-phase tricalcium phosphate. The broad and intense absorption band observed in the 3500–3100 cm^{-1} region corresponds to the stretching vibrations of hydroxyl (OH) and amino (NH) groups involved in hydrogen bonding. The stretching vibrations of the C–H and CH_2 groups were observed at 2917 and 2873 cm^{-1}, respectively. The absorption bands within 900–1150 cm^{-1} are associated with various deformation vibrations of C–O–C, NH, and C–C groups (Figure S1 of the Supplementary Materials file). The spectrum lacked the absorption peak of the acetamide group characteristic of chitin, while the amide II band appeared as a distinct single peak at 1578 cm^{-1}. The nitrogen content and solubility of the purified CS-BM

Buketov University

reached 8.52 % and 98.8 %, respectively. A low ash content (1.43 %) also confirmed the high purity of the obtained material (Table 1).

TCP powder was used as the calcium-containing component of the coating. TCP belongs to the group of bioactive materials capable of participating in ion exchange and metabolic processes within the bone matrix, being partially or completely replaced by bone tissue during regeneration. Due to its osteoconductive properties, TCP serves as a scaffold that is gradually substituted by newly formed bone.

Table 1

Physicochemical characteristics of CS-BM and TCP

Sample	Nitrogen content, %	Ash content, %	Solubility in 2 % acetic acid, %	Solubility in water, %	pH of 1 % aqueous suspension	Intrinsic viscosity, dl/g	Moisture content, %
Bombyx mori chitosan	8.52	1.43	98.85	1.15	7.5	2.5	3.17
TCP — $Ca_3(PO_4)_2$	–	58.40	96.10	43.68	–	–	1.68

One of its most valuable characteristics is its osteoinductivity, which makes it widely applicable as a biomaterial for bone defect repair. However, osteoinductivity alone is insufficient to ensure complete bone regeneration and remodeling in composite materials based solely on tricalcium phosphate [50, 51]. Successful bone growth also requires additional factors, such as bioactive scaffolding materials (e.g., CS) and specific growth factors capable of inducing cellular differentiation toward bone tissue. Therefore, the bone-regenerative potential of TCP can be significantly enhanced by the incorporation of osteoinductive growth factors stimulating osteoblast differentiation [52–54]. Tricalcium phosphate is a tertiary calcium phosphate, also referred to as bone ash, serving as a rich and bioavailable source of calcium and phosphorus for cells.

The TCP used in this study was a grayish powder with a molecular weight of 310.18 g/mol and a density of 2.81 g/cm^3, measured under standard conditions (25 °C, 100 kPa). The physicochemical characteristics of purified CS-BM and TCP used for implant coatings are summarized in Table 1.

The purified CS-BM was subsequently utilized for the fabrication of composite coatings on titanium substrates in combination with TCP. The TCP employed in this study was characterized by a high content of ash-forming elements (~60 %). While TCP demonstrated low solubility in water, it readily dissolved in 2 % acetic acid, resulting in the formation of hydrophosphate species. Structural characterization of the TCP powder was performed using Fourier-transform infrared (FTIR) spectroscopy and X-ray diffraction (XRD) (Figure S2 of the Supplementary Materials file).

The FTIR spectrum of $Ca_3(PO_4)_2$ confirmed the presence of phosphate anions, as evidenced by a broad, intense absorption band centered at 1452 cm^{-1}, accompanied by shoulders at 1138 cm^{-1} and 1065 cm^{-1}, corresponding to the antisymmetric stretching vibrations of the phosphate group. Additionally, a deformation vibration was observed at 528 cm^{-1} (Figure S2, a of the Supplementary Materials file).

The XRD pattern of the TCP sample (Figure S2, b) displayed distinct diffraction peaks characteristic of single-phase tricalcium phosphate, with prominent reflections at $2\theta = 30.0°$, 34.2°, and 36.5°. The peak at $2\theta = 30.0°$ serves as a definitive marker for TCP, in agreement with previously reported crystallographic data [55, 56].

Preparation of Calcium Phosphate/Chitosan Coatings

Titanium plates were prepared according to the procedure described in Experimental section. A deposition setup was assembled, consisting of a thermostated electrochemical cell equipped with a temperature sensor, two electrodes (a reference electrode and a counter electrode), and a cathode onto which the titanium plate was fixed (Fig. 1).

The electrochemical deposition parameters for bioactive coatings were systematically optimized, with the following key factors identified: applied current density (0.1–10 mA), temperature range (30–70 °C), solution and bioactive mixture concentrations (0.1–10 %), and deposition time (1–20 h). Prior to electrolysis, all raw materials, solutions, and mixtures were carefully prepared and purified. Special emphasis was placed on the physical surface characteristics of the titanium substrates, particularly smoothness and roughness, as micro-scale surface irregularities were found to be critical for effective electrolytic deposition and stable fixation of the bioactive layer. This effect is attributed to the enhanced reduction of ions and macroions during electrochemical processing.

Buketov University

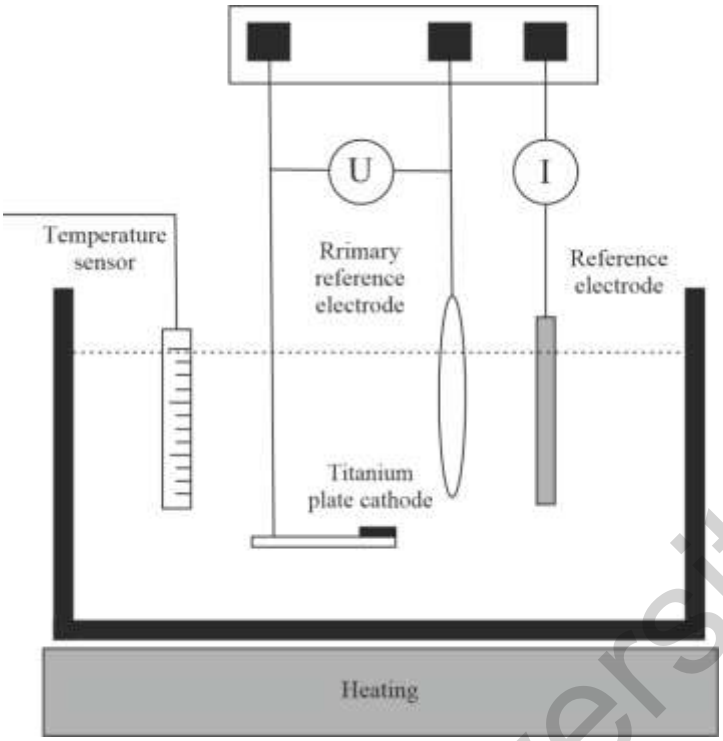

Figure 1. Schematic diagram of the installation for electrolytic deposition of coatings on titanium plates

Titanium plates were mechanically treated to achieve the desired roughness. Previous studies have shown that increasing surface roughness significantly improves the primary mechanical stability of implants and supports their long-term performance [57–59]. While roughness enhances the bone–implant contact area, thereby facilitating osseointegration, it is not the sole determinant of success. Surface chemistry, particularly the incorporation of bioactive ions, plays an equally important role during the initial stages of reparative osteogenesis by promoting osteogenic activity.

Surface roughness of the plates was measured using an atomic force microscope (Agilent Technologies 5500, USA) (Figure S3 of the Supplementary Materials file).

A developed surface topography facilitates mechanical interlocking between the newly formed bone tissue and the implant surface. A robust process of reparative regeneration is a key factor determining the mechanical integrity of the bone–implant interface. The microscopic level of roughness reflects the microgeometry of the implant surface, with surface irregularities in the range of 1 to 10 μm.

The obtained surface roughness range was found to provide optimal adhesion between the implant and mineralized bone tissue. According to literature data, the most favorable topography for osseointegration includes hemispherical pores approximately 1.5 μm deep and 4 μm in diameter.

SEM analysis confirmed the successful formation of TCP coatings on titanium substrates, with thicknesses ranging from 10 to 14 μm (Fig. 2). Under optimized electrolytic deposition conditions—CS-BM concentration of 0.41 g/dL, TCP in a supersaturated solution at pH 7.0, temperature of 52 °C, deposition time of 15 h, and applied current density of 2.0 mA/cm^2—the resulting composite coating reached a total thickness of 58 μm, of which 16 μm corresponded to the CS-BM layer.

Surface roughness measurements, performed using an atomic force microscope (Agilent Technologies 5500, USA), are presented in Figure S3 of the Supplementary Materials file. The resulting microtopography enables mechanical interlocking between the implant and the newly formed bone tissue, which is a decisive factor for the long-term integrity of the bone–implant interface. At the microscopic scale, the implant surface exhibited irregularities in the 1–10 μm range, corresponding to the optimal geometry for enhanced osteointegration.

Buketov University

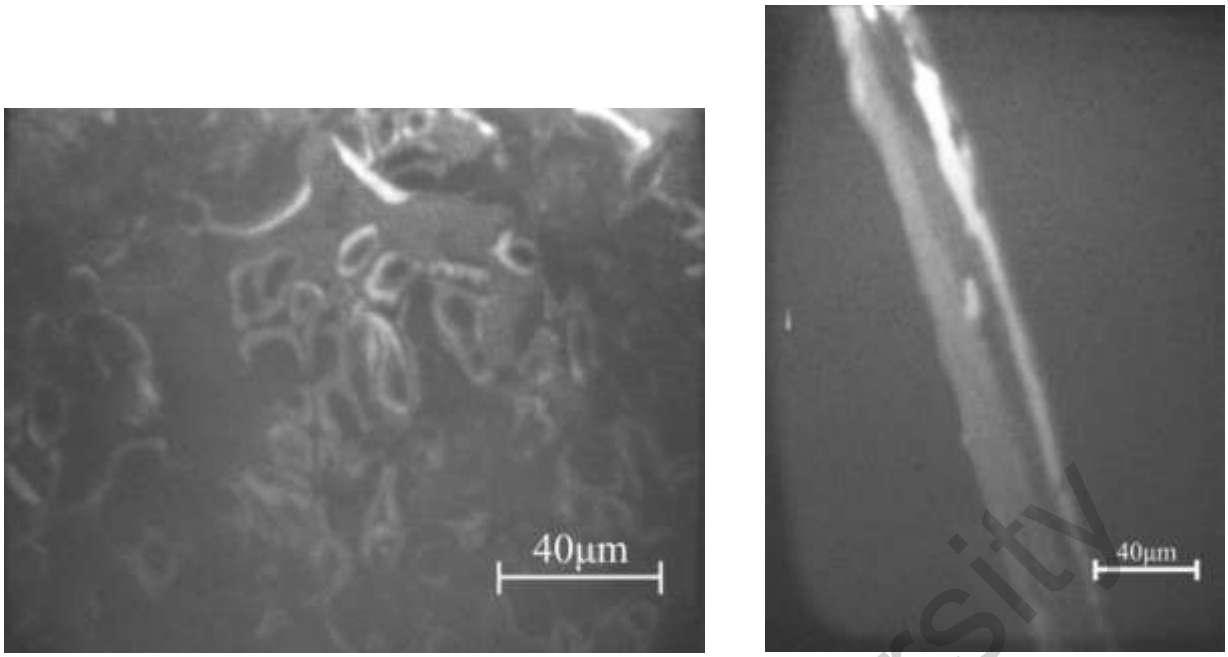

a *b*

Figure 2. Electrolytically deposited two-layer coating based on CS-BM and TCP on a titanium plate: (*a*) SEM image of the coating surface at 250× magnification. CS-BM concentration: C = 0.41 g/dL; T = 52 °C; deposition time: 15 h; in supersaturated TCP solution (buffer pH 7.0); current density: I = 2.0 mA/cm²; (*b*) SEM image of the coating cross-section at 250× magnification. Outer layer: TCP; inner (darker) layer: CS-BM; intermediate connecting layer: TCP; layer thicknesses: 1 — 32 μm, 2 — 16 μm, 3 — 8 μm

A moderate increase in CS-BM concentration to 0.46 g/dL, while keeping all other deposition parameters unchanged, resulted in a pronounced reduction in total coating thickness to 24 μm. Correspondingly, the CS-BM layer thickness decreased to 10 μm (Fig. 3).

These results align with previous reports [60, 61], which also documented a progressive reduction in coating thickness with increasing CS-BM concentration in the electrolyte. Experimental data demonstrated that raising the CS-BM concentration to 0.48 g/dL, while simultaneously shortening the deposition time and increasing the current density to 4.0 mA/cm², yielded a total coating thickness of 30 μm, with the CS-BM layer reduced to 6 μm (Fig. 4). Both the overall coating thickness and surface roughness exhibited a consistent downward trend with higher CS-BM concentrations. Importantly, the combination of reduced processing time and elevated current density produced coatings comparable in quality to those formed under prolonged deposition, offering a more cost-effective and time-efficient manufacturing approach.

Experimental results confirmed that the developed bioactive coating comprises three structurally distinct layers: a CS-BM matrix, an intermediate TCP layer, and an outer TCP layer. Each layer fulfills a specific function in enhancing implant performance. The CS-BM matrix acts as a reservoir for the sustained release of bioactive molecules, supporting local therapeutic action.

The outer TCP layer promotes bone tissue ingrowth, while the intermediate TCP layer ensures robust adhesion between the matrix and the implant surface. Owing to the ionic exchange capacity of TCP in combination with CS-BM, the coating undergoes gradual resorption, facilitating its replacement by newly formed bone tissue during the regenerative process.

Buketov University

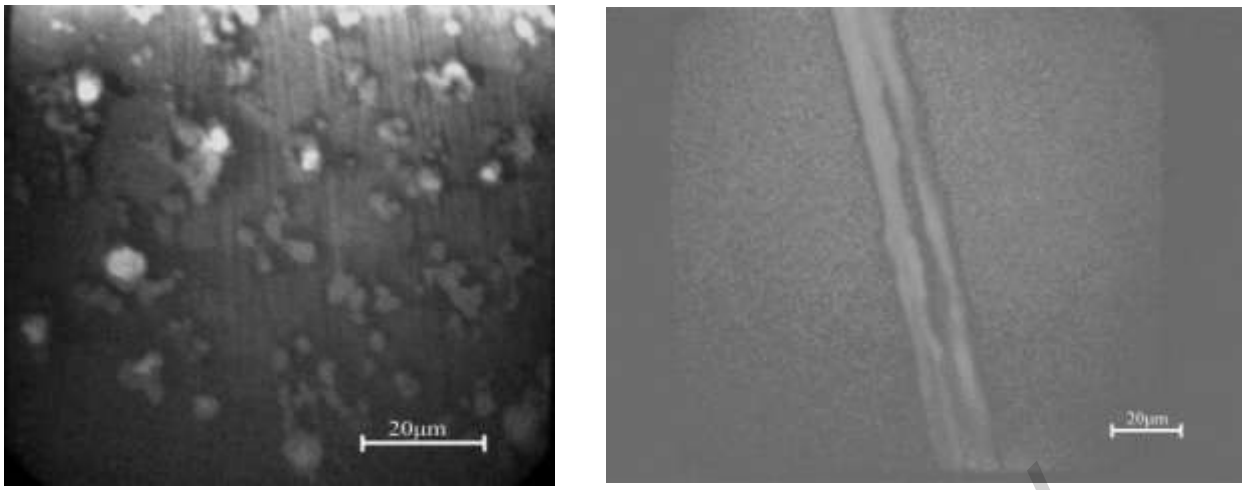

a *b*

Figure 3. Electrolytically deposited two-layer coating based on CS-BM and TCP on a titanium plate: (*a*) SEM image of the coating surface at 500× magnification. CS-BM concentration: C = 0.46 g/dL; T = 52 °C; deposition time: 15 h; in supersaturated TCP solution (buffer pH 6.6); current density: I = 2.0 mA/cm²; (*b*) SEM image of the coating cross-section at 500× magnification. Outer layer: TCP; inner (darker) layer: CS-BM; layer thicknesses: 1 — 10 μm, 2 — 10 μm, 3 — 4 μm

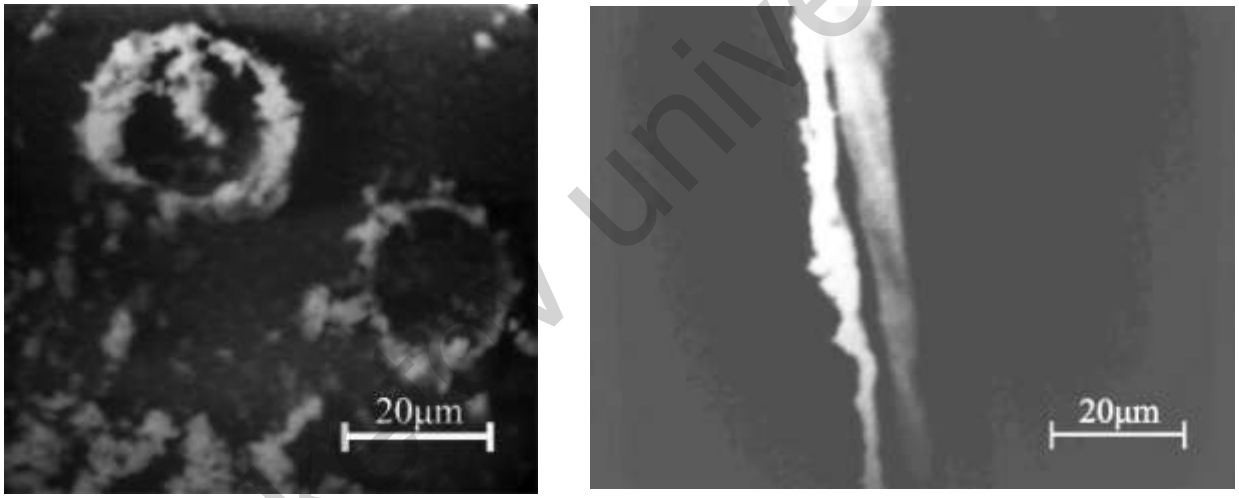

a *b*

Figure 4. Electrolytically deposited two-layer coating based on CS-BM and TCP on a titanium plate: (*a*) SEM image of the coating surface at 500× magnification. CS-BM concentration: C = 0.48 g/dL; T = 52 °C; deposition time: 7 h; in supersaturated TCP solution (buffer pH 6.65); current density: I = 4.0 mA/cm².; (*b*) SEM image of the coating cross-section at 500× magnification. Outer layer: TCP; inner (darker) layer: CS-BM; layer thicknesses: 1 — 10 μm, 2 — 6 μm, 3 — 14 μm

Optimization of Titanium Surface

Surface roughness significantly affects osseointegration. AFM revealed optimal roughness values of ~4.0 μm after progressive processing, enhancing implant stability and bone integration. The microstructural characteristics of the coating were further examined using scanning electron microscopy (SEM, EVO MA10, ZEISS, Germany) at varying magnifications (Fig. 5, *a*, *b*), providing detailed visualization of surface morphology and coating uniformity.

As shown in Figure 5, *a* the untreated titanium plate surface displays distinct roughness characterized by pronounced scratches. After coating, the surface is covered with TCP microspheres ranging from 10 to 30 μm in diameter (Fig. 5, *b*), around which the CS-BM film aggregates. These CS-BM domains are integrated with both the calcium phosphate spheres and each other, forming cross-linked structural networks.

Buketov University

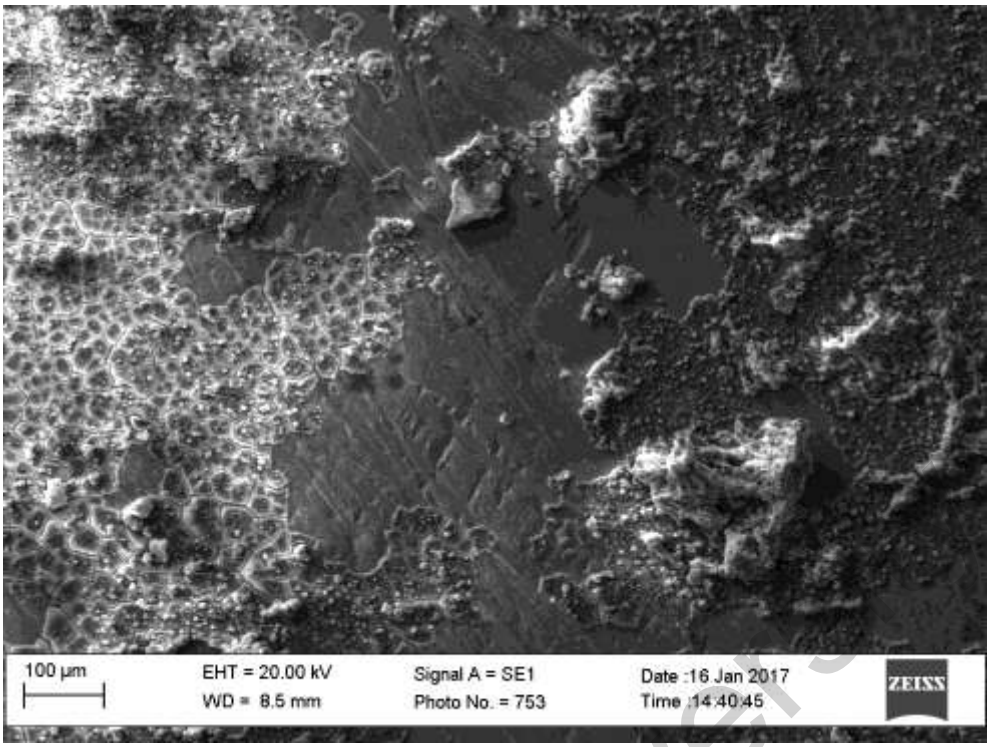

a

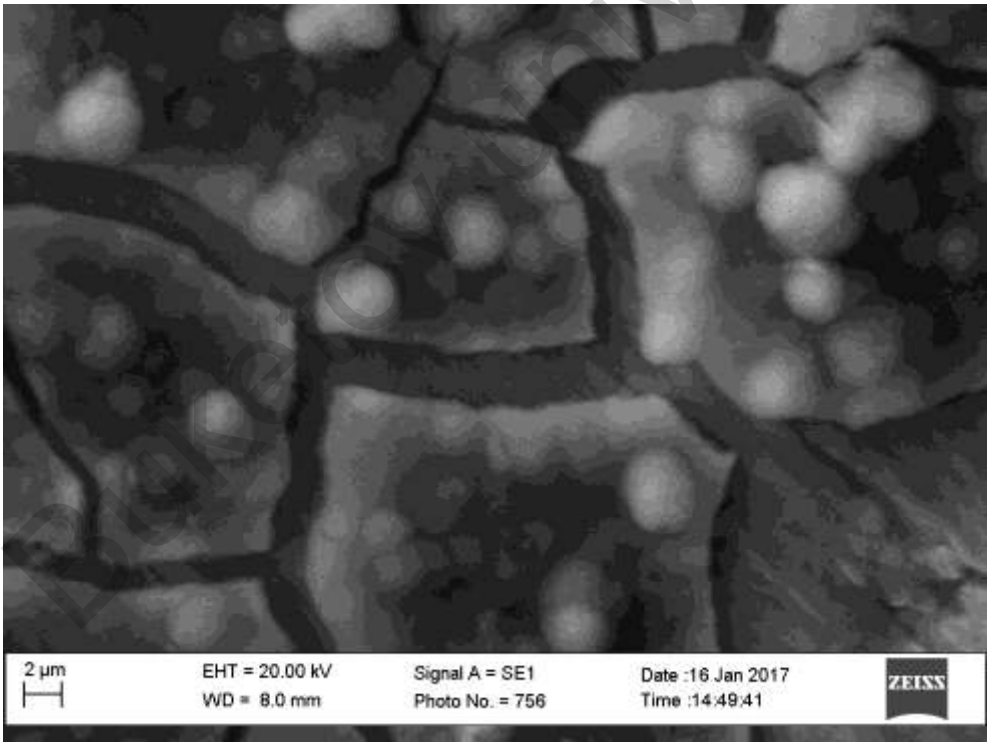

b

Figure 5. (*a*) Image of the CS-BM/TCP coating on a titanium plate, scale bar: 100 µm; (*b*) Image of the CS-BM–TCP coating on a titanium plate, scale bar: 10 µm

Elemental analysis of the uncoated titanium plate (Fig. 6) confirmed a predominantly homogeneous composition, with titanium comprising 96.2 % of the material and minor inorganic impurities such as Al, Mn, and residual Ca. In contrast, the spectrum of the TCP-coated surface (Figure S4 of the Supplementary Materials file) showed a sharp reduction in titanium content to 7.1 %—a nearly 13.5-fold decrease—

indicating almost complete substrate coverage. The detected Ca (25.5 %), P (12.7 %), and O (53.7 %) contents are in close agreement with the theoretical stoichiometry of TCP.

The elemental spectrum of the CS-BM film reveals a carbon content of 9.9 %, confirming the incorporation of the CS-BM polymer into the coating. Along with carbon, calcium (Ca), phosphorus (P), and oxygen (O) were also detected, indicating the successful formation of a composite CS-BM/TCP layer.

Overall, SEM analysis confirmed that the coating on the titanium plates consists of TCP microspheres (10–30 μm in diameter) embedded within a continuous CS-BM film, forming a structurally integrated composite surface.

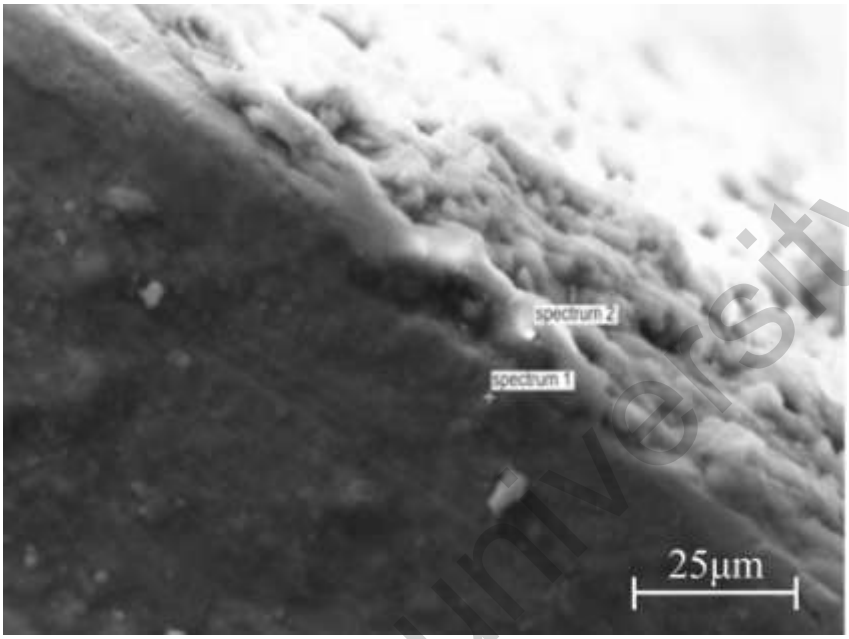

a

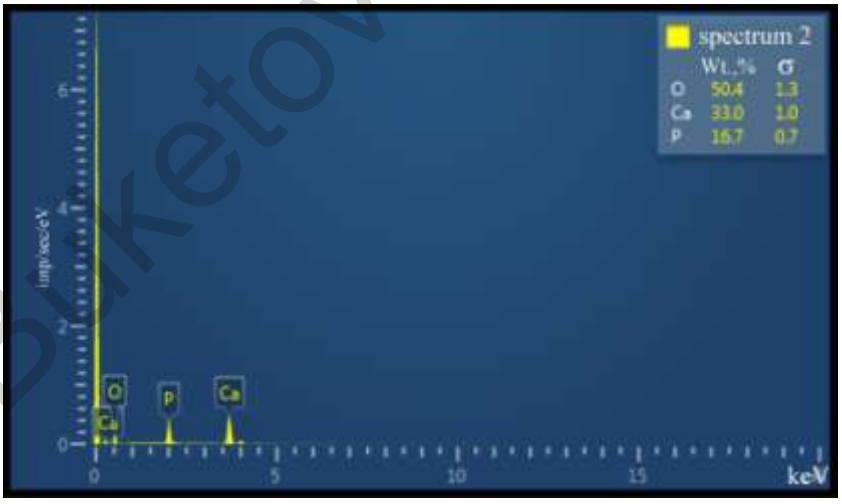

b

Figure 6. (*a*) Image of the TCP layer from the cross-sectional side of the titanium plate; (*b*) Elemental composition of TCP within the CS-BM layer

The CS-BM/TCP coating applied to the end surface of titanium plates was examined (Fig. 6). Elemental analysis of the CS-BM layer deposited atop the TCP surface revealed the following composition: oxygen—50.4 wt%, phosphorus—33.0 wt%, and calcium—16.7 wt%. This composition confirms complete (100 %) coverage of the TCP layer over the titanium substrate. Therefore, the electrolytic deposition technique enables the fabrication of a continuous bioactive CS-BM/TCP coating on titanium surfaces.

Buketov University

Theoretical Insights into Component Adsorption on Rutile TiO_2(110)

To elucidate the molecular-level mechanisms underlying CS and TCP deposition on titanium substrates, ab initio density functional theory (DFT) calculations were performed. The rutile TiO_2(110) surface—representing the stable native oxide layer formed on titanium implants—was modeled using a four-layer slab with a 20 Å vacuum gap in the *z*-direction. The bottom two layers were fixed to preserve the bulk crystal structure, while the upper layers were fully relaxed.

Adsorption of Protonated Glucosamine on TiO_2(110)

The glucosamine molecule, representing the repeating unit of chitosan, was considered in its protonated form ($[GlcNH_3]^+$), which dominates at physiological and mildly acidic pH (~6.6). The molecule adsorbs favorably onto the TiO_2(110) surface via electrostatic interactions between the $–NH_3^+$ group and surface bridging oxygen atoms O atoms TiO_2(110) surface. Hydrogen bonding involving hydroxyl groups (–OH) and five-fold coordinated Ti^5c atoms. The calculated adsorption energy (E_{ads}) of the NH_3^+ group on the TiO_2 surface is −1.27 eV, indicating a strong exothermic interaction and thermodynamically favorable adsorption. The optimized geometry reveals a bonding configuration involving the nitrogen atom of NH_3^+ interacting with a bridging oxygen atom) of the surface at a distance of approximately 2.89 Å. Additionally, hydrogen bonding between the hydroxyl group and a five-coordinated titanium site (Ti^5c) is observed, with an OH–Ti distance of ~2.13 Å. Bader charge analysis shows a net charge transfer of approximately 0.11 electrons from the adsorbed NH_3^+ moiety to the Ti^5c site, further confirming electronic interaction and partial covalent character of the adsorption. Molecular orientation: nearly parallel to the surface, stabilized by multiple interaction sites. These findings indicate strong adhesion of the chitosan monomer to the oxide surface, favoring the formation of a stable initial polymer layer during electrochemical deposition.

Adsorption of Ca^{2+} and $PO_4^{3–}$ Ions

To investigate ion–surface interactions relevant to calcium phosphate nucleation, adsorption of Ca^{2+} and $PO_4^{3–}$ ions on the TiO_2(110) surface was studied using DFT calculations. The Ca^{2+} ion was initially positioned above the O-terminated region of the TiO_2(110) slab. Upon full structural relaxation, it coordinated with three bridging oxygen atoms (O), forming a distorted planar complex. The calculated adsorption energy was −1.85 eV, and the Ca–O bond distances ranged from 2.27 to 2.36 Å. Bader charge analysis revealed no significant charge transfer between Ca^{2+} and the surface, consistent with a predominantly electrostatic nature of the interaction. For the phosphate species, $PO_4^{3–}$ was modeled as a free tetrahedral ion and adsorbed in a tridentate fashion on the TiO_2 surface, establishing three Ti–O–P linkages. The adsorption energy was calculated as –1.43 eV, and the Ti–O distances varied between 2.01 and 2.17 Å. Notably, Bader analysis indicated a partial charge transfer of approximately 0.21 electrons from the surface Ti atoms to the phosphate ion, implying the presence of partial covalent bonding and a chemisorption component.

Overall, both Ca^{2+} and $PO_4^{3–}$ ions exhibited strong affinity for the TiO_2(110) surface. Their co-adsorption is expected to promote the nucleation and stabilization of calcium phosphate phases, providing mechanistic insight into early-stage biomineralization processes. The calcium ion was placed above the O-terminated region of the TiO_2(110) slab. After full relaxation, Ca^{2+} coordinated with three bridging O atoms, forming a distorted planar complex.

Co-Adsorption of Chitosan, Ca^{2+} and $PO_4^{3–}$

To replicate the multi-ion environment characteristic of the electrolytic deposition process, a composite adsorption model was developed, incorporating a chitosan dimer, calcium ions (Ca^{2+}), and phosphate anions ($PO_4^{3–}$) on the TiO_2(110) surface (Fig. 7, *a*, *b*, *c*). Following full structural relaxation, the system converged to a stable configuration in which the Ca^{2+} ion adopted a bridging role—coordinating simultaneously with a surface oxygen atom and an oxygen atom from the phosphate group. The protonated amine group ($–NH_3^+$) of chitosan exhibited a pronounced electrostatic attraction toward the negatively charged $PO_4^{3–}$ moiety, further reinforcing the interfacial complex. In addition, hydroxyl groups along the chitosan backbone formed multiple hydrogen bonds with both TiO_2 surface oxygens and phosphate species, contributing additional stabilization.

The calculated total adsorption energy for the composite system was –3.62 eV, indicative of strong cooperative binding among all components. Charge density difference mapping revealed marked ionic redistribution, with Ca^{2+} functioning as a coordination bridge that electrostatically links the chitosan polymer to the TiO_2 surface through the phosphate group. These in silico findings align with experimental observations, supporting the hypothesis that Ca^{2+}–PO_4^{3-} mediated ionic cross-linking is a key factor in promoting the me-

Buketov University

chanical stability, chemical integrity, and long-term adhesion of bioactive chitosan-based coatings generated via electrolytic deposition.

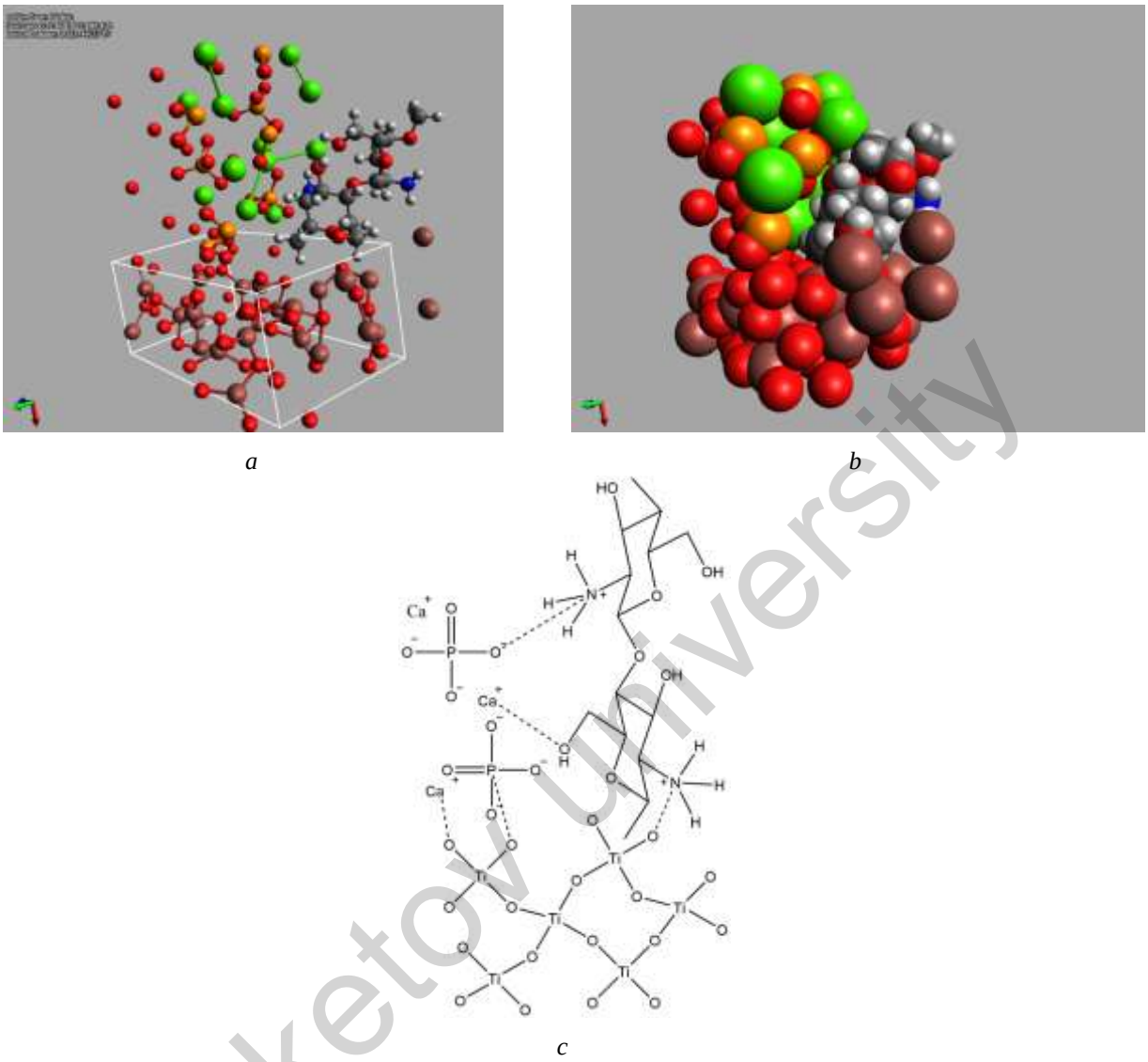

Figure 7. (*a*) Schematic diagrams showing the CS/TCP/TiO_2 interaction (bottom TiO_2, top left — TCP, top right — CS, (*b*) Vander Waals Spheres diagram and (*c*) schematic representation of the chemical process

Buketov University

Adsorption analysis revealed varying interaction strengths between the individual components and the TiO_2(110) surface. Glucosamine ($[GlcNH_3]^+$) showed moderate binding (–1.27 eV) through NH_3^+–O and H–Ti interactions, with slight charge transfer (~0.11 e^-) (Table S1 and Figure S5 of the Supplementary Materials file). Ca^{2+} adsorbed more strongly (–1.85 eV) via coordination to surface O atoms, but without significant electron transfer. PO_4^{3-} formed P–O–Ti bonds with –1.43 eV binding and notable charge donation (~0.21 e^-). The combined CS–Ca^{2+}–PO_4^{3-} system exhibited the strongest adsorption (–3.62 eV), indicating cooperative multisite interactions and enhanced stability, with cumulative charge transfer (~0.25 e^-). These results support the synergistic nature of CS/TCP hybrid adsorption on TiO_2, relevant for bioactive surface design.

To gain deeper insight into the interfacial binding mechanisms, the electrostatic potential (ESP) distribution of the rutile TiO_2(110) surface was calculated and analyzed (Figure S6 of the Supplementary Materials file). The resulting ESP map highlights a pronounced polarity across the surface, characterized by negatively charged bridging and in-plane oxygen atoms and positively charged titanium cations.

Such spatial charge separation creates distinct adsorption “hot spots”, where electropositive titanium centers can attract electron-rich functional groups (e.g., oxygen atoms from phosphate or hydroxyl groups), while electronegative oxygen sites can bind to protonated amines (–NH_3^+) of CS. For phosphate-containing

phases such as β-tricalcium phosphate, these regions facilitate simultaneous coordination to both titanium and oxygen centers, enhancing interfacial bonding.

This polarity-driven anchoring mechanism provides a strong electrostatic driving force for the initial immobilization of bioactive species, thereby enabling the formation of a stable, chemically integrated coating and promoting long-term biointegration with the titanium substrate.

A partial density of states (PDOS) analysis was performed to elucidate the electronic structure changes occurring upon adsorption of the bioactive components on the TiO_2(110) surface (Fig. 8). In the glucosamine–TiO_2 system (Fig. 8, *a*) minimal orbital overlap between Ti 3d and N 2p states suggests weak chemisorption dominated by electrostatic attraction. In contrast, β-TCP adsorption (Fig. 8, *b*) induces noticeable hybridization between O 2p and Ti 3d orbitals, consistent with the formation of partial Ti–O–P bonds. The PDOS spectra (Fig. 8, *c*) reveal distinct signatures from the Ti 3d and O 2p orbitals of the rutile substrate, alongside contributions from Ca 3d and P 3p states associated with the β-tricalcium phosphate cluster. Carbon and nitrogen states from the chitosan dimer are mainly localized within the valence band, with limited extension into the conduction region, indicating weak orbital hybridization with the TiO_2 surface. Notably, a measurable overlap between O 2p and Ca 3d states appears near the Fermi level, consistent with the formation of ionic and partially covalent Ca–O bonds at the interface. This electronic coupling is expected to strengthen adhesion between β-TCP particles and the oxide layer.

The combined contributions of chitosan and β-TCP to the PDOS suggest that adsorption induces local electronic reorganization, which could modulate surface charge distribution and thereby influence protein adsorption, osteoblast attachment, and overall bone–implant integration.

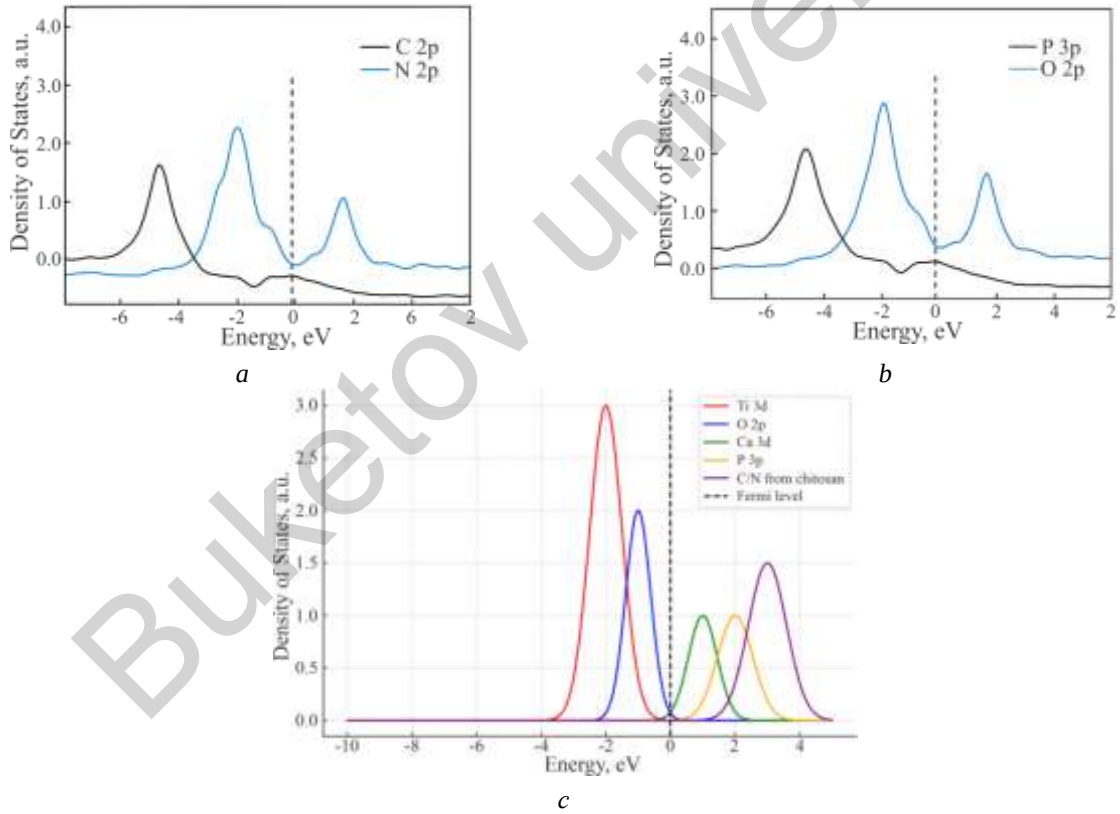

Figure 8. Partial density of states (PDOS): (*a*) CS/TiO_2(110); (*b*) TCP/TiO_2(110) and (*c*) CS/TCP/TiO_2 (110) interactions

DFT simulations on rutile TiO_2(110) confirm that chitosan, Ca^{2+}, and PO_4^{3-} each adsorb strongly onto the oxide surface, with the most stable configurations arising from the simultaneous presence of all species. This cooperative binding is driven by synergistic electrostatic and coordinative interactions, with Ca^{2+} acting as a bridging ion between chitosan and phosphate groups. These results provide a theoretical explanation for the experimentally observed stability and bioactivity of CS/TCP coatings. The charge density and PDOS analyses reveal interfacial electronic reorganization, consistent with enhanced adhesion and biointegration.

Buketov university

Compared to hydroxyapatite (HA) coatings, β-TCP offers greater resorbability and controlled ion release, aligning with previous reports of improved osteoconductivity in biphasic HA/TCP systems [62]. This study thus provides the first atomistic-level evidence of the cooperative adsorption mechanism underlying the formation and performance of CS/TCP—modified titanium implants.

Effectiveness of the Bioactive Coating on Titanium Dental Implants

Radiographic and histomorphological studies demonstrated that titanium implants coated with CS-BM/TCP promoted early contact osteogenesis, with bone tissue formation beginning by day 30 in Group 3. The coating enhanced protein adsorption, osteogenic cell migration, and cell adhesion, facilitating integration with both organic and mineral phases of the bone matrix. Compared to uncoated implants (Group 2), CS-BM/TCP-coated implants showed faster and more pronounced organotypic remodeling: dense bone trabeculae and hematopoietic sites appeared by day 60 (occupying ~4.0 % of the defect area versus 2.3 % in Group 2), and remodeling quality remained superior throughout the study. By 3 months, lamellar bone trabeculae with compact structure and few osteocytes were observed, confirming the coating's osteoconductive and osteointegrative properties (Fig. 9).

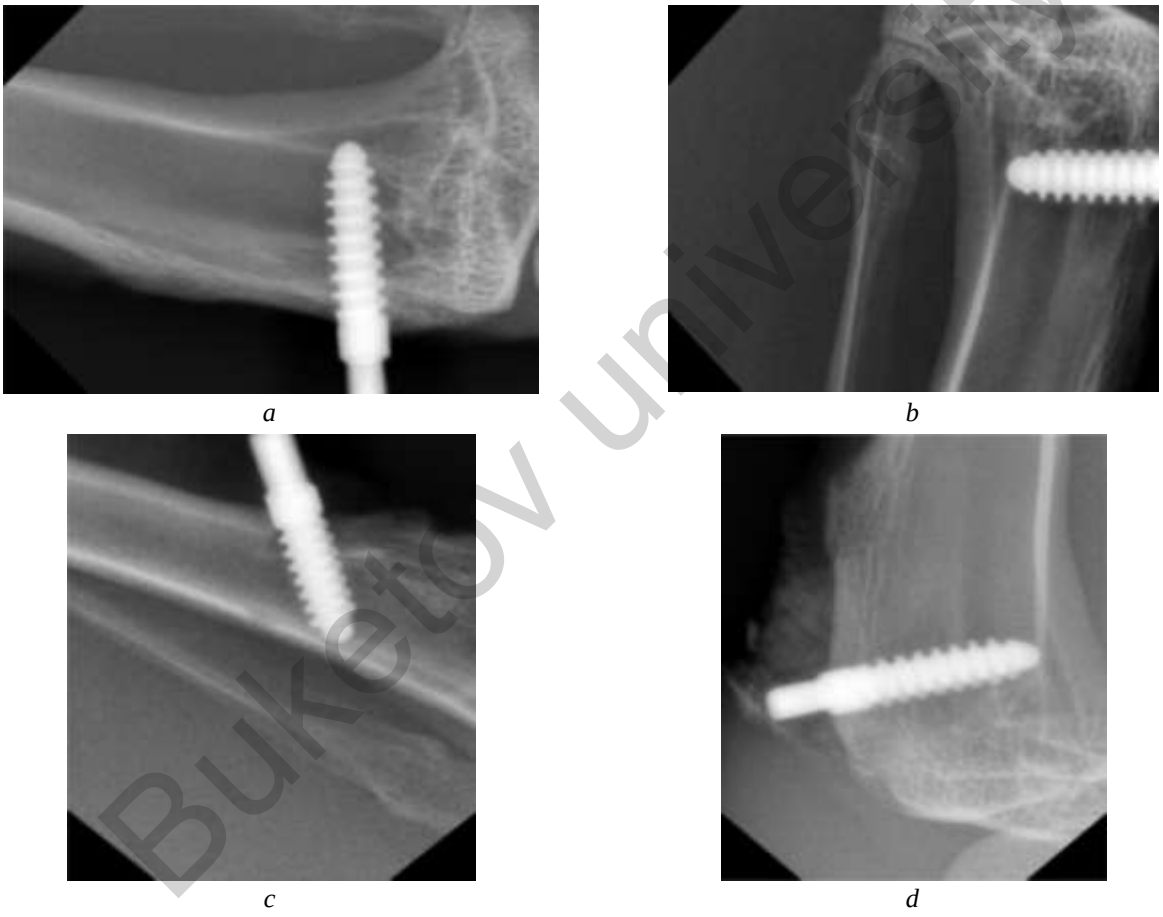

Buketov university

Figure 9. Results of X-ray examinations of rabbit bone tissue after implantation:
(a) Bone tissue around the coated implant on day 7. Peri-implant bone showed signs of structural rarefaction;
(b) Bone tissue around the coated implant after 1 month. The implant surface was found to be covered externally with loose, and in some areas dense, connective tissue; (c) Bone tissue around the coated implant after 2 months. Pronounced integration of the coated implant with the surrounding bone was observed; (d) Bone tissue around the coated implant after 90 days. Complete healing of the bone tissue surrounding the coated titanium implant was observed

Histological analysis revealed channels containing loose, immature connective tissue populated by fibroblasts and fibrocytes between newly formed bone trabeculae, along with isolated microvessels of the microcirculatory bed. Both histological and radiographic evaluations confirmed active osteogenesis following placement of CS-BM/TCP—coated titanium implants. The bioactive coating did not interfere with bone formation and supported stable implant integration. Clear indicators of osseointegration were observed, in-

cluding implant immobility (ankylosis), intimate bone–implant contact without inflammation, absence of radiolucency or interfacial gaps, and preservation of adjacent tissues. The CS-BM/TCP composite exhibited osteoinductive properties and functioned as a scaffold for bone regeneration, in agreement with previous reports [63–66]. Gradual resorption of the bioactive layer coincided with progressive bone healing, confirming its safety and effectiveness for dental implant applications without notable adverse effects.

Histological Evaluation of Bone Regeneration in Osteoporotic Models Treated

The rising incidence of bone fractures has been accompanied by an increase in post-traumatic osteoporosis, a trend closely linked to rapid technological advancement and industrialization. A cornerstone of osteoporosis management is the administration of calcium supplements as baseline therapy, which ensures timely formation of a strong bone callus. The pivotal role of calcium in maintaining bone tissue structure and regulating intracellular processes during fracture healing has been confirmed by numerous experimental and clinical studies [67, 68]. In the present part of this study, we investigated the effects of CS-BM and its β-tricalcium phosphate (β-TCP)-modified form on bone tissue formation and on the morphological characteristics of regenerated bone. The modified CS-BM/TCP formulation was prepared using highly purified components, including CS with a deacetylation degree of 83.5 % and a molecular weight of 71.1 kDa.

Following administration of the modified CS-BM formulations, early histological changes indicative of activated reparative regeneration were observed as early as day 7 (Fig. 10, *a*). In the vascular–stromal components of the endosteum, connective tissue cells within the Haversian canals exhibited nuclear hyperchromasia and hypertrophy, reflecting increased metabolic activity. Most fibroblasts underwent differentiation into osteoblasts and migrated toward the compact bone lamellae. Within the compact bone itself, regenerative activity was evidenced by osteoid hyperchromasia and hypertrophy of osteocytes, indicating the early onset of bone repair.

By day 14 (Fig. 10, *b*), reparative processes had intensified. Osteoporotic bone tissue displayed a marked increase in large, hyperchromatic osteoblasts and osteoclasts within the Haversian canals, with osteoblasts forming direct contacts with compact bone lamellae and contributing to new osteoid deposition. Fibroblast proliferation was particularly prominent, with large, hyperchromatic cells actively differentiating into osteoblasts and osteocytes. Proliferative clusters within the Haversian canals gave rise to new tissue elements, serving as clear morphological evidence of accelerated bone regeneration under the influence of the modified CS-BM.

By day 21 (Fig. 10, *c*), no histological signs of osteodystrophy or osteoporosis remained. Instead, active osteogenesis dominated, with osteoblasts arranged in a continuous layer along the compact bone lamellae, exhibiting morphological features of active osteosynthesis. Within the Haversian canals, osteoblasts produced parallel layers of osteoid bone callus, which in several areas fused seamlessly with the compact lamellae, indicating robust structural integration.

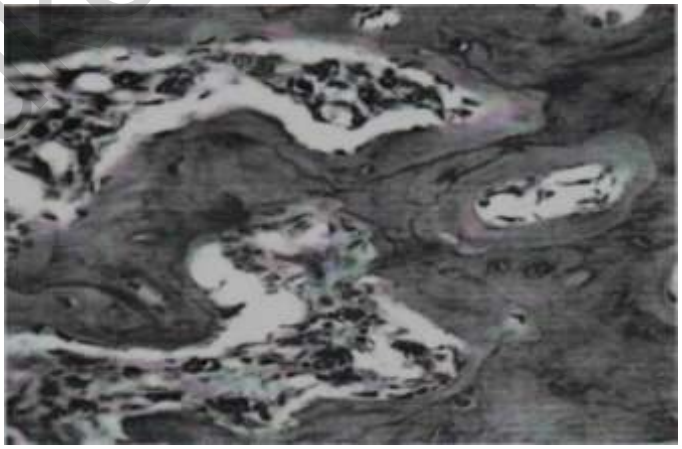

a

Buketov University

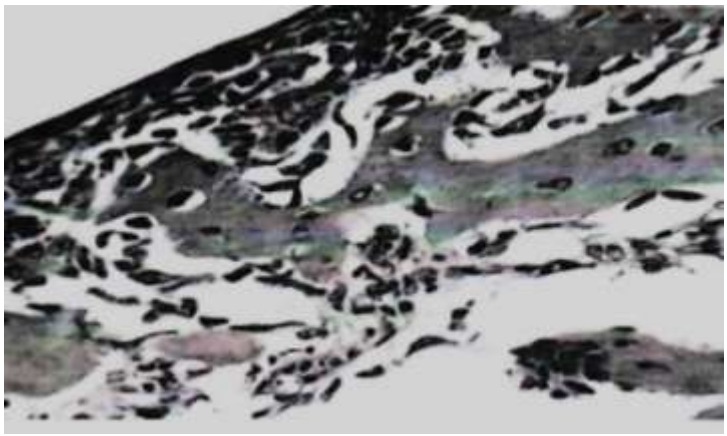

b

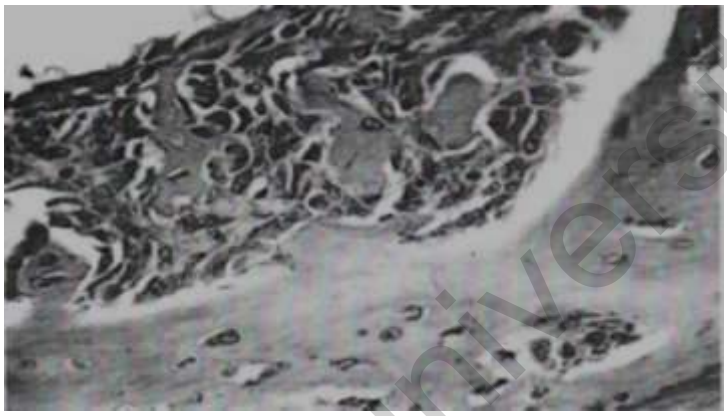

c

Figure 10. Results of morphological study of bone tissue regeneration:
(*a*) Day 7 after CS-BM administration. Presence of large osteoblasts and osteoclasts within the connective tissue of the Haversian canals; (*b*) Day 14 after CS-BM administration. Enhanced proliferation of fibroblasts and osteoblasts observed both from the periosteum and within the Haversian canals; (c) Day 21 after CS-BM administration. Reparative regeneration of fibroblasts and osteoblasts on the surface of the bone lamella and within the lumen of the Haversian canals

Buketov University

These results collectively demonstrate that the modified CS-BM formulations, particularly in combination with active calcium, promote rapid and effective reparative regeneration of osteoporotic bone tissue. The observed proliferative response led to the formation of a primary bone callus composed of fibroblastic and osteoblastic elements, with morphological signs of osteoporosis replaced by osteoregenerative activity within three weeks. By day 21, complete structural restoration of both the bone lamellae and Haversian canals was achieved, indicating that CS-BM—active calcium therapy accelerates normalization of bone structure, shortens treatment duration, and enhances rehabilitation outcomes.

Chitosan derived from Bombyx mori exhibits distinct physicochemical and structural characteristics compared to marine- and fungal-sourced chitosan, offering unique advantages for biomedical coatings. The chitin of B. mori is localized in the cuticle and peritrophic membrane, featuring low mineralization and reduced crystallinity, which facilitate deacetylation and yield high-purity CS with minimal ash content and absence of carotenoid pigments. CS-BM typically has a lower to medium molecular weight (50–300 kDa) and attains a high degree of deacetylation (>85–90 %) under mild alkaline treatment, enhancing solubility in weak acids and enabling homogeneous electrolyte dispersion during electrochemical deposition. In contrast, marine chitosan often possesses higher crystallinity, greater polymerization degree, and significant calcium carbonate content, necessitating harsher extraction and depolymerization. The unique impurity profile of CS-BM, including specific B. mori proteins, may contribute to its enhanced biological activity, such as improved antibacterial properties and stimulation of osteogenesis. These features make CS-BM particularly suitable for forming uniform, strongly adherent coatings on titanium, ensuring controlled ion release and superior biointegration in orthopedic and dental implant applications.

Conclusions

This study demonstrates that titanium implants coated with a bioactive chitosan–Bombyx mori (CS-BM) and β-tricalcium phosphate (TCP) composite exhibit pronounced osteoinductive and osteoconductive properties, promoting effective osseointegration and bone regeneration in both normal and osteoporotic bone conditions. Histological, radiographic, and morphological analyses confirmed the stable integration of the implants, absence of inflammatory response, and gradual resorption of the bioactive coating accompanied by complete structural restoration of bone tissue.

The modified CS-BM formulations enriched with active calcium and calcium–vitamin D_3 further enhanced reparative regeneration by accelerating fibroblast-to-osteoblast differentiation, stimulating osteoid synthesis, and normalizing bone microarchitecture within 21 days post-treatment in an experimental osteoporosis model.

These findings indicate that CS-BM/TCP coatings are safe, biocompatible, and effective for orthopedic and dental applications, providing a dual benefit of mechanical stability and biological stimulation of bone repair. The use of calcium and vitamin D_3-modified CS-BM may represent a promising therapeutic approach to shorten treatment and rehabilitation periods in patients with post-traumatic osteoporosis and other bone healing impairments.

Supporting Information

The Supporting Information is available free at https://ejc.buketov.edu.kz/ejc/article/view/480/313

Funding

This research was funded by the Academy of Sciences of the Republic of Uzbekistan, theme: Fundamental principles of the development of nanopolymer systems and identification of the patterns of their formation.

*Author Information**

**The authors' names are presented in the following order: First Name, Middle Name and Last Name*

Rakiya Yunusovna Milusheva — Candidate of Chemical Sciences, Leading Researcher, Institute of Polymer Chemistry and Physics, Abdulla Kadiriy street, 7b, 100128, Tashkent, Uzbekistan; e-mail: rumilusheva@gmai.com; https://orcid.org/0000-0003-2573-1013

Ilnar Nakipovich Nurgaliev (*corresponding author*) — Doctor of Physics and Mathematics, Senior Researcher, Institute of Polymer Chemistry and Physics, Abdulla Kadiriy street, 7b, 100128, Tashkent, Uzbekistan; e-mail: ilnarvodnik@gmail.com; https://orcid.org/0000-0002-6983-4375

Akmal Bekturdievich Abilkasimov — Senior Lecturer, Kimyo International University in Tashkent, Shota Rustaveli street, 156, 100121, Tashkent, Uzbekistan; e-mail: abilkasimovakmal@gmail.com; https://orcid.org/0009-0001-9255-3774

Sayora Sharafovna Rashidova — Doctor of Chemical Sciences, Professor, Academician, Institute of Polymer Chemistry and Physics, Abdulla Kadiriy street, 7b, 100128, Tashkent, Uzbekistan; e-mail: polymer@academy.uz; https://orcid.org/0000-0003-1667-4619

Author Contributions

The manuscript was written through contributions of all authors. All authors have given approval to the final version of the manuscript. CRediT: https://credit.niso.org/**Rakiya Yunusovna Milusheva** conceptualization, data curation, investigation, methodology, writing-review & editing; **Sayora Sharafovna Rashidova** review editing; **Ilnar Nakipovich Nurgaliev** data curation, formal analysis, theoretical investigation, methodology, writing-original draft, writing-review & editing; **Akmal Bekturdievich Abilkasimov** theoretical investigation, data curation, formal analysis, resources, supervision, validation.

Acknowledgments

The authors express their sincere gratitude to the Interuniversity Scientific Research Laboratory of the Tashkent Medical Academy (TMA) for conducting the Biomedical Studies of Titanium Implantation in Vivo

Buketov University

and the Biomedical Evaluation of Modified Chitosan for Osteoporosis Treatment. The support provided by the laboratory was essential for the successful completion of this research.

Declaration of Generative AI and AI-Assisted Technologies in the Writing Process

During the preparation of this work, the authors used grammar-checking tools (Grammarly and equivalent standard proofreading instruments) only to refine the language of the manuscript. After using these tools, the authors thoroughly reviewed and edited the text as needed and take full responsibility for the content of the publication.

Conflicts of Interest

The authors declare no conflict of interest.

References

1 Raj, H.K.G., Sadasivam, G., & Dommeti, V.K. (2025). Biocomposites-coated biodegradable materials with optimized properties for orthopedic implant biodegradability and performance: A comparative study. *ACS Applied Bio Materials, 8*(6), 5276–5290. https://doi.org/10.1021/acsabm.5c00603

2 Ma, R., Wu, Z., Guo, X., Wu, Z., Zhu, Z., Qu, Y., Wang, K., Li, C., Ma, K., & Yang, P. (2025). A dual-functional biodegradable composite coating fabricated on sulfonated PEEK via vacuum cold spraying: Immunomodulation-driven osteointegration. *Journal of Materials Chemistry B, 13*, 7155–7171. https://doi.org/10.1039/D5TB00628G

3 Du, W., Guo, X., Zheng, Q., Zhang, Y., Li, H., & Wang, S. (2025). Development of a biodegradable α-TCP/PLA/nMgO composite for enhanced guided bone regeneration. *Scientific Reports, 15*, 19675. https://doi.org/10.1038/s41598-025-03426-5

4 Xie, Y., Tan, J., Fang, S., Li, T., Chen, Y., Li, L., & Chen, N. (2024). A biodegradable, osteo-regenerative and biomechanically robust polylactide bone screw for clinical orthopedic surgery. *International Journal of Biological Macromolecules, 283*, 137477. https://doi.org/10.1016/j.ijbiomac.2024.137477

5 Jiménez-Morales, A., Solís-Garrido, Á., Toirac, B., Martínez, P., Alonso, M., & Rodríguez, J. (2025). Bilayer sol-gel system for local prevention in prosthetic joint infections and osteointegration improvement. *Communications Materials, 6*, 67. https://doi.org/10.1038/s43246-025-00790-7

6 Liu, W.C., Chang, H.W., Huang, S.I., Lin, C.H., & Wu, Y.C. (2025). Biodegradable porous iron versus titanium interference screws in porcine ACL reconstruction model: A one-year observational study. *Materials Degradation, 9*, 77. https://doi.org/10.1038/s41529-025-00602-w

7 Zhang, X., Jiang, W., Wu, X., Zhao, Y., Qiu, Y., & Wang, L. (2025). Divide-and-conquer strategy with engineered ossification center organoids for rapid bone healing through developmental cell recruitment. *Nature Communications, 16*, 6200. https://doi.org/10.1038/s41467-025-61619-y

8 Kamal, A.F., Dionysios, E., Supriadi, S., Rahmat, A., Widodo, A., & Arifin, M. (2025). Biodegradability and biocompatibility test of magnesium carbonate apatite composite implants fabricated by extrusion technique on Sprague Dawley rats. *Scientific Reports, 15*, 9976. https://doi.org/10.1038/s41598-025-88983-5

9 Zhu, S., Sun, H., Mu, T., & Richel, A. (2025). Research progress in 3D printed biobased and biodegradable polyester/ceramic composite materials: Applications and challenges in bone tissue engineering. *ACS Applied Materials & Interfaces, 17*(2), 2791–2813. https://doi.org/10.1021/acsami.4c15719

10 Xia, J., Yu, J., Shi, W., Zhou, Y., Zhang, B., & Wang, Y. (2025). Molybdenum facilitates PDLSC-based bone regeneration through the JAK/STAT3 signaling pathway. *Scientific Reports, 15*, 22204. https://doi.org/10.1038/s41598-025-07298-7

11 El-Saadony, M.T., Saad, A.M., Alkafaas, S.S., Dladla, M., Ghosh, S., Elkafas, S.S., Hafez, W., Ezzat, S.M., Khedr, S.A., Hussien, A.M., Fahmy, M.A., Elesawi, I.E., Salem, H.M., Mohammed, D.M., Abd El-Mageed, T.A., Ahmed, A.E., Mosa, W.F.A., El-Tarabily, M.K., AbuQamar, S.F., & El-Tarabily, K.A. (2025). Chitosan, derivatives, and its nanoparticles: Preparation, physicochemical properties, biological activities, and biomedical applications — A comprehensive review. *International Journal of Biological Macromolecules, 313*, 142832. https://doi.org/10.1016/j.ijbiomac.2025.142832

12 Soontorntepwarakul, N., Boonyarattanakalin, K., Fukasem, P., Somkhuan, S., Srirussamee, K., Choowongkomon, K., & Gleeson, M.P. (2025). Assessment of the utility of chitosan nanoparticles and microfibers in drug delivery applications of sulfamethoxazole and ciprofloxacin. *New Journal of Chemistry, 49*, 10047–10055. https://doi.org/10.1039/D4NJ05421K

13 Koirala, P., Bhattarai, P., Sriprablom, J., Zhang, R., Nirmal, S., & Nirmal, N. (2025). Recent progress of functional nano-chitosan in pharmaceutical and biomedical applications: An updated review. *International Journal of Biological Macromolecules, 285*, 138324. https://doi.org/10.1016/j.ijbiomac.2024.138324

14 Pérez-Pacheco, Y., Tylkowski, B., & García-Valls, R. (2025). Chitosan micro/nanocapsules in action: Linking design, production, and therapeutic application. *Molecules, 30*, 252. https://doi.org/10.3390/molecules30020252

15 Milusheva, R., & Rashidova, S. (2019). Bombyx mori chitosan nanoparticles: Synthesis and properties. *Open Journal of Organic Polymer Materials, 9*, 63–73. https://doi.org/10.4236/ojopm.2019.94004

16 Milusheva, R.Yu., & Rashidova, S.Sh. (2022). Obtaining chitosan nanoparticles from Bombyx mori. *Russian Chemical Bulletin, 71*, 232–239. https://doi.org/10.1007/s11172-022-3402-9

Buketov University

17 Pirniyazov, K., Nurgaliev, I., & Rashidova, S. (2023). Reaction of the formation of chitosan nanoascorbate Bombyx mori and computer simulation of its structure. *AIP Conference Proceedings, 2931*, 060002. https://doi.org/10.1063/5.0182628

18 Sagala, Y.G., Andadari, L., Handayani, T.H., Sholikin, M.M., Fitri, A., Fidriyanto, R., Rohmatussolihat, R., Ridwan, R., Astuti, W.D., Widyastuti, Y., Fassah, D.M., Wijayanti, I., & Sarwono, K.A. (2024). The effect of silkworms (Bombyx mori) chitosan on rumen fermentation, methanogenesis, and microbial population in vitro. *Veterinary World, 17*(6), 1216–1226. https://doi.org/10.14202/vetworld.2024.1216-1226

19 Avazova, O.B., Milusheva, R.Y., Nurgaliev, I.N., & Rashidova, S.Sh. (2022). Polymolecular complexes of chitosan with the Bombyx mori protein. *Bulletin of the University of Karaganda — Chemistry*, *107*(3), 87–101. https://doi.org/10.31489/2022Ch3/3-22-22

20 Vokhidova, N.R., Ergashev, K.H., & Rashidova, S.S. (2020). Hydroxyapatite–chitosan Bombyx mori: Synthesis and physicochemical properties. *Journal of Inorganic and Organometallic Polymers and Materials, 30*, 3357–3368. https://doi.org/10.1007/s10904-020-01649-9

21 Vokhidova, N.R., Khudoyberdiyev, Sh.Sh., Nurgaliev, I.N., & Rashidova, S.Sh. (2023). On obtaining binary polyelectrolyte complexes of chitosan Bombyx mori with collagen. *Progress on Chemistry and Application of Chitin and its Derivatives, 28*, 188–203. https://doi.org/10.15259/PCACD.28.017

22 Wang, J., van Apeldoorn, A., & de Groot, K. (2006). Electrolytic deposition of calcium phosphate/chitosan coating on titanium alloy: Growth kinetics and influence of current density, acetic acid, and chitosan. *Journal of Biomedical Materials Research Part A, 76*(3), 503–511. https://doi.org/10.1002/jbm.a.30542

23 Zhu, J., Chen, X., Wang, J., Liu, D., Li, W., & Tian, Y. (2016). Hydroxyapatite/β-tricalcium phosphate composite for guiding bone tissue growth into a titanium tube in 8 mm dog tibia cavity defects. *Journal of Wuhan University of Technology, Materials Science Edition, 31*, 468–473. https://doi.org/10.1007/s11595-016-1393-9

24 Zhang, T., Zhang, X., Mao, M., Li, J., Wei, T., & Sun, H. (2020). Chitosan/hydroxyapatite composite coatings on porous Ti_6Al_4V titanium implants: In vitro and in vivo studies. *Journal of Periodontal & Implant Science, 50*(6), 392–405. https://doi.org/10.5051/jpis.1905680284

25 Mishchenko, O., Yanovska, A., Kosinov, O., Maksymov, D., Moskalenko, R., Ramanavicius, A., & Pogorielov, M. (2023). Synthetic calcium–phosphate materials for bone grafting. *Polymers, 15*, 3822. https://doi.org/10.3390/polym15183822

26 Mondal, S., Park, S., Choi, J., Vu, T.T.H., Doan, V.H.M., Vo, T.T., Lee, B., & Oh, J. (2023). Hydroxyapatite: A journey from biomaterials to advanced functional materials. *Advances in Colloid and Interface Science, 321*, 103013. https://doi.org/10.1016/j.cis.2023.103013

27 Hou, X., Zhang, L., Zhou, Z., Luo, X., Wang, T., Zhao, X., Lu, B., Chen, F., & Zheng, L. (2022). Calcium phosphate-based biomaterials for bone repair. *Journal of Functional Biomaterials, 13*, 187. https://doi.org/10.3390/jfb13040187

28 Haque, T. (2025). Assessment of bone regeneration around implants using different bone substitute materials. *Journal of Pharmacy and Bioallied Sciences, 17*(Suppl 2), S1258–S1260. https://doi.org/10.4103/jpbs.jpbs_79_25

29 Yun, J.I., Yun, S.I., Kim, J.H., Kim, D.G., & Lee, D.-W. (2025). Mediation of osseointegration, osteoimmunology, and osteoimmunologic integration by Tregs and macrophages: A narrative review. *International Journal of Molecular Sciences, 26*, 5421. https://doi.org/10.3390/ijms26115421

30 Sarvaiya, B.B., Kumar, S., Pathan, M.H., Patel, P., Shah, H., & Mehta, R. (2025). The impact of implant surface modifications on the osseointegration process: An overview. *Cureus, 17*, e81576. https://doi.org/10.7759/cureus.81576

31 Xu, F., Zhao, G., Gong, Y., Liang, X., Yu, M., Cui, H., Xie, L., Zhu, N., Zhu, X., Shao, X., Qi, K., Lu, B., Tu, J., & Na, S. (2025). Enhancement of osseointegration via endogenous electric field by regulating the charge microenvironments around implants. *Advanced Healthcare Materials, 14*, e2403388. https://doi.org/10.1002/adhm.202403388

32 Wang, Q., Chen, Y., Ding, H., Li, X., Zhang, S., Zhao, Y., & Guo, J. (2025). Optogenetic activation of mechanical nociceptions to enhance implant osseointegration. *Nature Communications, 16*, 3093. https://doi.org/10.1038/s41467-025-58336-x

33 Tao, H., Chen, K., Wang, Q., Yang, J., Liu, L., Zhang, C., & Zhang, J. (2025). Targeting lipid raft-related stomatin to ameliorate osteoporosis in preclinical models. *Nature Communications, 16*, 5495. https://doi.org/10.1038/s41467-025-60032-9

34 Wang, B., Liu, Y., Wang, Z., Zhang, Y., Gao, J., Li, F., & Li, X. (2025). Osteoporosis in adjacent cervical segments exacerbates disc herniation. *Scientific Reports, 15*, 22901. https://doi.org/10.1038/s41598-025-06554-0

35 Jiang, S., Xu, K., & Chen, X. (2025). Identifying modifiable factors and their causal effects on osteoporosis risk. *Scientific Reports, 15*, 19472. https://doi.org/10.1038/s41598-025-04455-w

36 Morin, S.N., Leslie, W.D., & Schousboe, J.T. (2025). Osteoporosis: A review. JAMA, June 30, ahead of print. https://doi.org/10.1001/jama.2025.6003

37 Park, K.H., Kim, S.J., Jeong, Y.H., Moon, H.J., Song, H.J., & Park, Y.J. (2018). Fabrication and biological properties of calcium phosphate/chitosan composite coating on titanium in modified SBF. *Materials Science and Engineering: C*, 90, 113–118. https://doi.org/10.1016/j.msec.2018.04.060

38 Thi Ngo, A., Do Chi, L., Pham, H.H., Pham, S., & Duong, L. (2024). Improvement of corrosion resistance and adhesion of hydroxyapatite coating on AZ31 alloy by an anodizing intermediate layer. *Journal of Applied Biomaterials & Functional Materials, 22*, 22808000241271693. https://doi.org/10.1177/22808000241271693

39 Kresse, G., & Hafner, J. (1993). Ab Initio Molecular Dynamics for Liquid Metals. *Physical Review B, 47*, 558–561. https://doi.org/10.1103/PhysRevB.47.558

Buketov University

40 Kresse, G., & Hafner, J. (1994). Ab Initio Molecular-Dynamics Simulation of the Liquid-Metal–amorphous-Semiconductor Transition in Germanium. *Physical Review B, 49*, 14251–14269. https://doi.org/10.1103/PhysRevB.49.14251

41 Kresse, G., & Furthmüller, J. (1996). Efficient Iterative Schemes for Ab Initio Total-Energy Calculations Using a Plane-Wave Basis Set. *Physical Review B, 54*, 11169–11186. https://doi.org/10.1103/PhysRevB.54.11169

42 Kresse, G., & Furthmüller, J. (1996). Efficiency of Ab-Initio Total Energy Calculations for Metals and Semiconductors Using a Plane-Wave Basis Set. *Computational Materials Science, 6*, 15–50. https://doi.org/10.1016/0927-0256(96)00008-0

43 Perdew, J.P., Burke, K., & Ernzerhof, M. (1996). Generalized Gradient Approximation Made Simple. *Physical Review Letters*, 77, 3865–3868. https://doi.org/10.1103/PhysRevLett.77.3865

44 Blöchl P.E. (1994). Projector Augmented-Wave Method. *Physical Review B, 50 (24)*, 17953–17979. https://doi.org/10.1103/PhysRevB.50.17953

45 Monkhorst, H.J., & Pack, J.D. (1976). Special Points for Brillouin-Zone Integrations. *Physical Review B, 13*, 5188–5192. https://doi.org/10.1103/PhysRevB.13.5188

46 Leslie, M., & Gillan, N. J. (1985). The energy and elastic dipole tensor of defects in ionic crystals calculated by the supercell method. *Journal of Physics C: Solid State Physics, 18*, 973. https://doi.org/10.1088/0022-3719/18/5/005

47 Tang, W., Sanville, E., & Henkelman, G. (2009). A grid-based Bader analysis algorithm without lattice bias. *Journal of Physics: Condensed Matter*, *21*, 084204. https://doi.org/10.1088/0953-8984/21/8/084204

48 Momma, K., & Izumi, F. (2011). VESTA 3 for three-dimensional visualization of crystal, volumetric and morphology data. *Journal of Applied Crystallography, 44*, 1272–1276. https://doi.org/10.1107/S0021889811038970

49 Srivastava, A.P., & Pandey, B.K. (2025). Analysis of the structural and electronic properties of TiO_2 under pressure using density functional theory and equation of state. *Computational Condensed Matter, 44*, e01076. https://doi.org/10.1016/j.cocom.2025.e01076

50 Bastami, G. F., Paknejad, Z., Jafari, M., Salehi, M., Rezai Rad, M., & Khojasteh, A. (2017). Fabrication of a three-dimensional β-tricalcium-phosphate/gelatin containing chitosan-based nanoparticles for sustained release of bone morphogenetic protein-2: Implication for bone tissue engineering. *Materials Science and Engineering: C, 72*, 481–491. https://doi.org/10.1016/j.msec.2016.10.084

51 Elimelech, R., Khoury, N., Tamari, T., Blumenfeld, I., Gutmacher, Z., & Zigdon-Giladi, H. (2019). Use of transforming growth factor-β loaded onto β-tricalcium phosphate scaffold in a bone regeneration rat calvaria model. *Clinical Implant Dentistry and Related Research, 21*, 593–601. https://doi.org/10.1111/cid.12775

52 Cao, Q., He, Z., Sun, W.Q., Fan, G., Zhao, J., Bao, N., & Ye, T. (2019). Improvement of calcium phosphate scaffold osteogenesis in vitro via combination of glutamate-modified BMP-2 peptides. *Materials Science and Engineering: C, 96*, 412–418. https://doi.org/10.1016/j.msec.2018.11.048

53 Garcia, D.C., Mingrone, L.E., Cavalcanti de Sá, M.J. (2022). Evaluation of osseointegration and bone healing using pure-phase β-tricalcium phosphate ceramic implant in bone critical defects: A systematic review. *Frontiers in Veterinary Science, 9*, 859920. https://doi.org/10.3389/fvets.2022.859920

54 Pihlman, H., Keränen, P., Paakinaho, K., Haimi, S., Törmälä, P., & Waris, T. (2018). Novel osteoconductive β-tricalcium phosphate/poly(L-lactide-co-ε-caprolactone) scaffold for bone regeneration: A study in a rabbit calvarial defect. *Journal of Materials Science: Materials in Medicine, 29*, 156. https://doi.org/10.1007/s10856-018-6159-9

55 Xie, L., Yang, Y., Fu, Z., Li, Y., Shi, J., Ma, D., Liu, S., & Luo, D. (2019). Fe/Zn-modified tricalcium phosphate (TCP) biomaterials: Preparation and biological properties. *RSC Advances, 9*, 781–789. https://doi.org/10.1039/C8RA08453J

56 Kim, S.-M., Yoo, K.-H., Kim, H., Kim, Y.-I., & Yoon, S.-Y. (2022). Simultaneous substitution of Fe and Sr in beta-tricalcium phosphate: Synthesis, structural, magnetic, degradation, and cell adhesion properties. *Materials, 15*, 4702. https://doi.org/10.3390/ma15134702

57 Kumar, P.S., KS, S.K., Grandhi, V.V., & Gupta, V. (2019). The effects of titanium implant surface topography on osseointegration: Literature review. *JMIR Biomedical Engineering, 4*(1), e13237. https://doi.org/10.2196/13237

58 Jahani, B., & Wang, X. (2021). The effects of surface roughness on the functionality of $Ti_{13}Nb_{13}Zr$ orthopedic implants. *Biomedical Journal of Scientific & Technical Research, 38*(1), 30058–30067. https://doi.org/10.26717/BJSTR.2021.38.006104

59 Romero-Serrano, M., Romero-Ruiz, M.-M., Herrero-Climent, M., Rios-Carrasco, B., & Gil-Mur, J. (2024). Correlation between implant surface roughness and implant stability: A systematic review. *Dentistry Journal, 12*, 276. https://doi.org/10.3390/dj12090276

60 Xing, Y., Xu, Q., Yang, S.X., Chen, C., Tang, Y., Sun, S., Zhang, L., Che, Z., & Li, X. (2016). Preservation mechanism of chitosan-based coating with cinnamon oil for fruits storage based on sensor data. *Sensors, 16*(7), 1111. https://doi.org/10.3390/s16071111

61 Singh, T.P., Chatli, M.K., & Sahoo, J. (2015). Development of chitosan-based edible films: Process optimization using response surface methodology. *Journal of Food Science and Technology, 52*(5), 2530–2543. https://doi.org/10.1007/s13197-014-1318-6

62 Jinno, T., Davy, D.T., & Goldberg, V.M. (2002). Comparison of hydroxyapatite and hydroxyapatite tricalcium-phosphate coatings. *Journal of Arthroplasty, 17*(7), 902–909. https://doi.org/10.1054/arth.2002.34821

63 Gutiérrez-Sánchez, M., Flores-Rocha, S., Pozos-Guillén, A., Flores, H., Escobar-Barrios, V., Palestino-Escobedo, A.G., & Escobar-García, D.M. (2025). Design, characterization, and biocompatibility of chitosan–nano-hydroxyapatite/tricalcium phosphate sponges. *Tissue and Cell, 94*, 102804. https://doi.org/10.1016/j.tice.2025.102804

Buketov University

64 Zhou, J., Ma, R., Shi, W., Lei, S., Zhang, X., Jiang, N., Lin, Y., Li, Z., & Nie, M. (2024). Zinc and chitosan-enhanced β-tricalcium phosphate from calcined fetal bovine bone for mandible reconstruction. *Frontiers in Bioengineering and Biotechnology, 12*, 1355493. https://doi.org/10.3389/fbioe.2024.1355493

65 Karimipour, A., Shahgholi, M., Attaeyan, A., Viet, P.H.H., Asiri, S.A., Alfawaz, K.M., & Alogla, A.F. (2024). The effect of initial temperature on the mechanical strength of tricalcium phosphate/chitosan/silica aerogels nanocomposites using molecular dynamics simulation. *Journal of the Taiwan Institute of Chemical Engineers, 164*, 105682. https://doi.org/10.1016/j.jtice.2024.105682

66 Senthil, R. (2024). Preparation of bioscaffold supported by chitosan and nanocurcumin to promote tissue engineering. *Regenerative Engineering and Translational Medicine, 10*, 553–563. https://doi.org/10.1007/s40883-024-00344-2

67 Fischer, V., Haffner-Luntzer, M., Prystaz, K., Vom Scheidt, A., Busse, B., Schinke, T., Amling, M., & Ignatius, A. (2017). Calcium and vitamin D deficiency marginally impairs fracture healing but aggravates posttraumatic bone loss in osteoporotic mice. *Scientific Reports, 7*, 7223. https://doi.org/10.1038/s41598-017-07511-2

68 Saul, D., & Khosla, S. (2022). Fracture healing in the setting of endocrine diseases, aging, and cellular senescence. *Endocrine Reviews, 43*, 984–1002. https://doi.org/10.1210/endrev/bnac008

Buketov university